Experimental observation of hydroelastic three-wave interactions

Luc Deike,[1,2] Michael Berhanu,[3] and Eric Falcon[3]
[1]*Department of Mechanical and Aerospace Engineering, Princeton University, New Jersey 08544, USA*
[2]*Princeton Environmental Institute, Princeton University, New Jersey 08544, USA*
[3]*Université Paris Diderot, Sorbonne Paris Cité, MSC, UMR 7057 CNRS, F-75013 Paris, France*
(Received 28 February 2017; published 30 June 2017)

We study experimentally three-wave interactions between hydroelastic waves propagating on the surface of a fluid covered by an elastic sheet (where both tension and bending are important). We observe the generation of a resonant daughter wave by nonlinear interaction among two mother waves of almost perpendicular directions. By using local and spatiotemporal wave-height measurements, the frequency and wave vector of the daughter wave are found to satisfy the resonance conditions within the measurement accuracy. Its amplitude is also found to be reasonably well described by the resonant wave interaction theory. Finally, a phase-locking among interacting waves is also observed, as expected theoretically.

DOI: 10.1103/PhysRevFluids.2.064803

I. INTRODUCTION

Nonlinear interactions are of fundamental interest to understand energy exchanges in wave systems. The first step in building a statistical theory of weakly nonlinear interactions such as weak turbulence is to identify the dominant type of interaction, i.e., the minimal number N of wave modes in the resonant interaction process [1,2].

Three-wave resonant interaction is the simplest weakly nonlinear process implying energy exchange between waves since it involves the smallest possible number of waves [3]. This type of nonlinear interaction has therefore been the subject of numerous theoretical studies in various physical contexts: plasma physics, nonlinear optics [4,5], and hydrodynamics [6–9]. Recent experiments have confirmed the occurrence of three-wave interaction for internal waves in a stratified flow [10–12] and in a rotating flow [13]. The case of capillary waves at a liquid surface has been widely studied, both experimentally and theoretically [14–17]. Occurrence of three-wave interactions at wave scales close to the gravity-capillary transition have also been reported [18–20]. Surface gravity waves have been the scope of numerous studies related to their importance in oceanography and it was shown experimentally and theoretically that three-wave interactions are forbidden by the dispersion relation (the resonant conditions cannot be fulfilled) and consequently the leading nonlinear process is four-wave interactions [6,7,21–23]. For elastic waves on a thin plate, the symmetry of the system also forbids three-wave interactions, and four-wave interactions are theoretically expected [24]. In real experimental systems, defaults and d-cones on the plate can lead to a mixture of three- and four-wave interactions [25]. Finally, more exotic systems, such as one-dimensional surface gravity waves, nonlinear optics, or Kelvin waves on vortex filaments are expected to have $N = 5$ or $N = 6$ as dominant resonant interaction processes [1].

Here, we present an experimental investigation of three-wave interactions on a floating elastic sheet that follows a previous study on nonlinear hydroelastic waves [26], where tension waves and flexural (or bending) waves are present, resulting from the coupling of the elastic sheet with the underneath fluid [6,7,14,27]. Hydroelasticity is defined by the coupling of the elastic medium (here the elastic sheet) with the hydrodynamics of the surrounding fluid. The results of the present study are discussed in the framework of *resonant wave interaction theory.* Hydroelastic waves are found in various domains: biomedical applications such as heart valves [28], flapping flags [29], very large floating structures [30], and on the surface of lakes or oceans covered by ice [31–33].

 ©2017 American Physical Society

In the context of hydroelastic waves, three-wave interactions are expected due to the form of the nonlinear boundary conditions [26,34] and were studied theoretically in Refs. [35,36]. We present an experimental confirmation of this prediction by using a simple, specifically designed experiment: two mother wave trains at slightly different angular frequencies ω_1 and ω_2 are generated in order to observe the formation of a daughter wave at the expected resonant frequency $\omega_3 = \omega_1 + \omega_2$. The geometrical resonant condition on the wave vectors $\mathbf{k}_3 = \mathbf{k}_1 + \mathbf{k}_2$ is also observed experimentally within some broadening. The time evolution of the daughter wave is recorded to access both its phase and its amplitude as a function of the amplitude of the mother waves. Its growth rate is discussed in the framework of resonant wave interaction theory. We conclude on the existence of three-wave interactions in hydroelastic waves in the range of scales where tension and bending are important.

This paper is organized as follows: Section II recalls the basics of wave interaction theory in the context of hydroelastic waves. The experimental setup is described in Sec. III. The experimental results of three-wave interactions are presented in Sec. IV, before drawing our conclusions in Sec. V.

II. RESONANT WAVE INTERACTION THEORY FOR HYDROELASTIC WAVES

A. Nonlinearity of system and dispersion relation

We consider a floating elastic sheet subjected to a uniform and isotropic tension T. The properties of the sheet are density ρ_e, Young's modulus E, Poisson modulus ν, and thickness h. The fluid density is ρ and its depth beneath the sheet at rest is H. The momentum equation of the thin elastic sheet is then given by [37–39]

$$D\nabla^4\eta - T\nabla^2\eta + \rho_e h\frac{\partial^2\eta}{\partial t^2} = p, \tag{1}$$

where η is the vertical sheet deformation, p is the pressure due to the liquid on the elastic sheet, $D \equiv \frac{Eh^3}{12(1-\nu^2)}$ is the bending modulus of the elastic sheet, and $\nabla^2 \equiv \partial^2/\partial x^2 + \partial^2/\partial y^2$ and $\nabla^4 \equiv \partial^4/\partial x^4 + \partial^4/\partial y^4 + 2\partial^4/\partial x^2\partial y^2$ are the Laplacian and bi-Laplacian operators, respectively. We consider an irrotational flow of velocity potential $\phi(x,y,z,t)$; the pressure equation on the surface $z = \eta$ is

$$p(x,y,t) = \rho g\eta + \frac{\partial\phi}{\partial t} + \rho\frac{v^2}{2}, \tag{2}$$

with $v \equiv \partial\eta/\partial t$ being the vertical velocity. For a plane-wave solution for η, using the kinematic boundary condition on the sheet surface $\frac{\partial\eta}{\partial t} = \frac{\partial\phi}{\partial z}_{z=\eta} = \tanh kH(\phi)_{z=\eta}$, and assuming negligible sheet inertia ($\rho_e kh/\rho \ll 1$) and infinite depth ($kH \gg 1$), the linear dispersion relation is

$$\omega^2 = gk + \frac{T}{\rho}k^3 + \frac{D}{\rho}k^5. \tag{3}$$

It involves three terms: a gravity term and two elastic terms. The second term of the right-hand member of Eq. (3) is a tension term structurally analogous to a capillary term, whereas the third term corresponds to bending. Note that the dispersion relation for pure elastic waves on a plate is $\omega^2 \sim Tk^2 + Dk^4$ [37], Eq. (3) coming from the coupling of the sheet elasticity with the underneath liquid. As discussed in Ref. [26], in our experiment, the crossover between gravity and tension waves is $\lambda_{gT} = 2\pi\sqrt{T/(g\rho)} \simeq 10$ cm; and between bending and tension waves, $\lambda_{\mathrm{TD}} = 2\pi\sqrt{D/T} \simeq 1$ cm. Note that, for ice floes, the bending elastic term prevails over the tension term, and the order of magnitude of the flexural-gravity transition is $\lambda_{gD} = 2\pi[D^\star/(g\rho)]^{1/4} \simeq 100$ m for a typical ice bending modulus $D^\star \approx 10^9$ N m [38,39]. Given the size of our experimental setup (40 cm) and the observation window (25×18 cm^2), gravity effects will be almost negligible (see Ref. [26] and Sec. III), and the dispersion relation thus reads [26]

$$\omega^2 = \frac{T}{\rho}k^3 + \frac{D}{\rho}k^5. \tag{4}$$

Thus the dispersion relation of tensional and bending waves is of decay type, i.e., $\omega \sim k^{\mu}$ with $\mu > 1$ (as for capillary waves), and therefore fulfills the three-wave resonance conditions on the frequency and the wave vectors [1]. As discussed in Ref. [26], while studying nonlinear hydroelastic waves in a wave turbulence regime, three-wave interactions occur when quadratic nonlinearities are present in the system whereas four-wave interactions have to be considered in the case of cubic nonlinearities [1]. The dynamics of wave interactions is dominated by the lowest nonlinear order in the weakly nonlinear limit [1]; thus, when three-wave and four-wave interactions occur, four-wave interactions can be neglected at leading order.

Nonlinearities involved in the system can be introduced either in the equations of the elastic plate, or in those of the fluid, or in the boundary condition between the fluid and the plate [34]. Although the equation for a single elastic plate involves cubic nonlinearities, the pressure term and the boundary condition between the fluid and the plate involves quadratic nonlinearities, with the pressure p. Therefore, as done by Ref. [36] in a Hamiltonian framework, three-wave interactions are expected to be dominant for any kind of hydroelastic wave and we consider them in the following.

Note that, in the case of pure flexural wave turbulence on an elastic plate (without water), four-wave interactions are considered since the nonlinearity of the plate are cubic [24]. For pure gravity waves, nonlinearities are quadratic but three-wave interactions are not possible since the resonant conditions are not satisfied due to the geometry of the dispersion relation ($\mu < 1$), and only four-wave interactions have to be considered [21].

B. General equations of three-wave interaction theory

We introduce the wave resonant interaction theory developed in the context of progressive capillary waves by McGoldrick [14] and generalized by Simmons [27], while the pioneer ideas were developed for ocean gravity surface wave by Phillips [6] and first observed in laboratory experiments by McGoldrick *et al.* [21], Longuet-Higgins and Smith [22], and more recently by Bonnefoy *et al.* [23]. The starting point is to consider resonant interactions between progressive wave modes as the leading energy exchange process for weak nonlinearity. In the case of quadratic nonlinearities, the leading interaction process involves three waves, and energy exchange between wave modes occurs if the spatial and temporal resonance conditions are fulfilled:

$$\begin{aligned} \omega_1 + \omega_2 - \omega_3 &= 0, \\ \mathbf{k}_1 + \mathbf{k}_2 - \mathbf{k}_3 &= 0. \end{aligned} \tag{5}$$

The wave vectors and frequencies are linked by the dispersion relation (4) in the case of hydroelastic waves with negligible gravity effects. Theoretically, the dispersion relation and the resonant conditions impose the angle between $\mathbf{k}_l$ and $\mathbf{k}_{l+1}$ for given frequencies.

We consider a generic wave system where three-wave interactions are possible, with two initial mother waves at frequency ω_1 and ω_2. Their resonant interactions gives birth to a daughter wave at frequency $\omega_3 = \omega_2 + \omega_1$. The general equation for a wave system containing three weakly nonlinear modes is given by [3,4,16,27]

$$\left(\frac{\partial}{\partial t} + U_j \cdot \boldsymbol{\nabla}\right) A_j + \delta_j A_j = i A_{j+1}^{*} A_{j+2}^{*} \gamma_j, \tag{6}$$

where i is the imaginary unit constant, δ_j is the temporal damping rate of wave j (assumed real), A_j is the complex amplitude (complex conjugates are denoted by *), U_j, is the group velocity, $j = 1,2,3$ is the circular array, and γ_j is the interaction coefficient. The interaction coefficient for gravity-capillary waves is given by [27]

$$\gamma_j = -\frac{k_j}{4\omega_j} \sum_{l=1}^{3} \omega_l \omega_{l+1} \left(1 + \frac{\mathbf{k}_l \cdot \mathbf{k}_{l+1}}{k_l k_{l+1}}\right). \tag{7}$$

The interaction coefficient depends on the structure of the nonlinear term, the wave geometry (through the scalar product $\mathbf{k}_l \cdot \mathbf{k}_{l+1}$), frequencies, and wave numbers, and thus implicitly on the physical properties of the wave propagation medium. The equations for gravity-capillary waves and gravity-tensional waves on a floating elastic sheet are exactly the same, surface tension being replaced by the sheet tension, so the work from Ref. [27] can be applied directly and the interaction coefficient is given by Eq. (7). In the weakly nonlinear approach, the bending term is linear with wave amplitude. The nonlinear terms due to the kinematic and dynamic boundary conditions are thus not modified by taking in account the bending waves. So we assume that we can use Eq. (7) for tension-bending waves, too. Note that adding bending changes the dispersion relation, which is taken into account in the interaction coefficient. Theoretically, the dispersion relation and the resonant conditions impose the angle between $\mathbf{k}_l$ and $\mathbf{k}_{l+1}$. Let us denote by $a_j(x,t)e^{i\phi_j(x,t)}$ a wave of amplitude a_j and phase $\phi_j \equiv \mathbf{k}_j \cdot \mathbf{x} - \omega_j t + \phi_j^0$, with ϕ_j^0 being an initial arbitrary phase. The evolution equations for the real amplitudes a_j and phases ϕ_j are, then, from Eq. (6),

$$\frac{\partial a_j}{\partial t} + \delta_j a_j + \nabla \cdot (U_j a_j) = a_{j+1} a_{j+2} \gamma_j \sin(\phi),$$
$$\frac{\partial \phi_j}{\partial t} + \nabla \cdot (U_j \phi_j) = \frac{a_{j+1} a_{j+2}}{a_j} \gamma_j \cos(\phi). \tag{8}$$

Note that we have introduced the total phase $\phi(x,t) \equiv \phi_1 + \phi_2 - \phi_3$. When the resonance conditions of Eq. (5) are satisfied, ϕ is reduced to the constant $\phi_1^0 + \phi_2^0 - \phi_3^0$. We now discuss stationary solutions of Eq. (8) under various hypotheses.

C. Theoretical daughter-wave amplitude and phase locking

We now focus on practical cases where two mother waves are forced at frequency ω_1 and ω_2 at a constant amplitude a_1 and a_2. The daughter wave has initially a zero amplitude and is expected to grow by pumping energy from the mother waves. We assume that the amplitude of the daughter wave remains small compared with the amplitude of the mother waves, $a_3 \ll a_1, a_2$, and that a_1 and a_2 are independent of time.

With no dissipation, and homogeneous wave field in Eqs. (8), the equations for the amplitude a_3 and phase Φ_3 of the daughter wave thus read

$$\frac{\partial a_3}{\partial t} = a_1 a_2 \gamma_3 \sin(\phi), \tag{9}$$
$$a_3 \frac{\partial \phi_3}{\partial t} = a_1 a_2 \gamma_3 \cos(\phi). \tag{10}$$

A phase locking between waves is expected since Eq. (10) reduces to $a_3 \partial_t \phi_3 = 0$ at the early stage of the resonance ($a_3 \approx 0$), and thus one should have $\phi = \pm\pi/2$. The total phase ϕ between waves is thus independent of time and is phase locked. Equation (9) then predicts that the amplitude a_3 of the daughter wave grows linearly in time at short times (i.e., for $a_3 \ll a_1$, a_2), and its growth rate is maximum when $\phi = -\pi/2$ since $\gamma_3 < 0$. The daughter initial phase is naturally set to $\phi_3^0 = -\pi/2 + \phi_1^0 + \phi_2^0$.

In presence of dissipation, and still with no spatial gradient term in Eqs. (8), a stationary solution of Eqs. (8) for the daughter-wave amplitude thus reads $a_3^S = a_1 a_2 \gamma_3 \sin\phi/\delta_3$. We now take into account the spatial term in Eqs. (8). A stationary solution for a_3 in the expected direction of the daughter wave, defined by O_ξ, given by $\mathbf{k_3}/||\mathbf{k_3}||$ (see sketch in Fig. 1), thus reads from Eq. (8)

$$U_3 \frac{\partial a_3^S}{\partial \xi} = a_1 a_2 \gamma_3 \sin\phi - \delta_3 a_3^S(\xi), \tag{11}$$

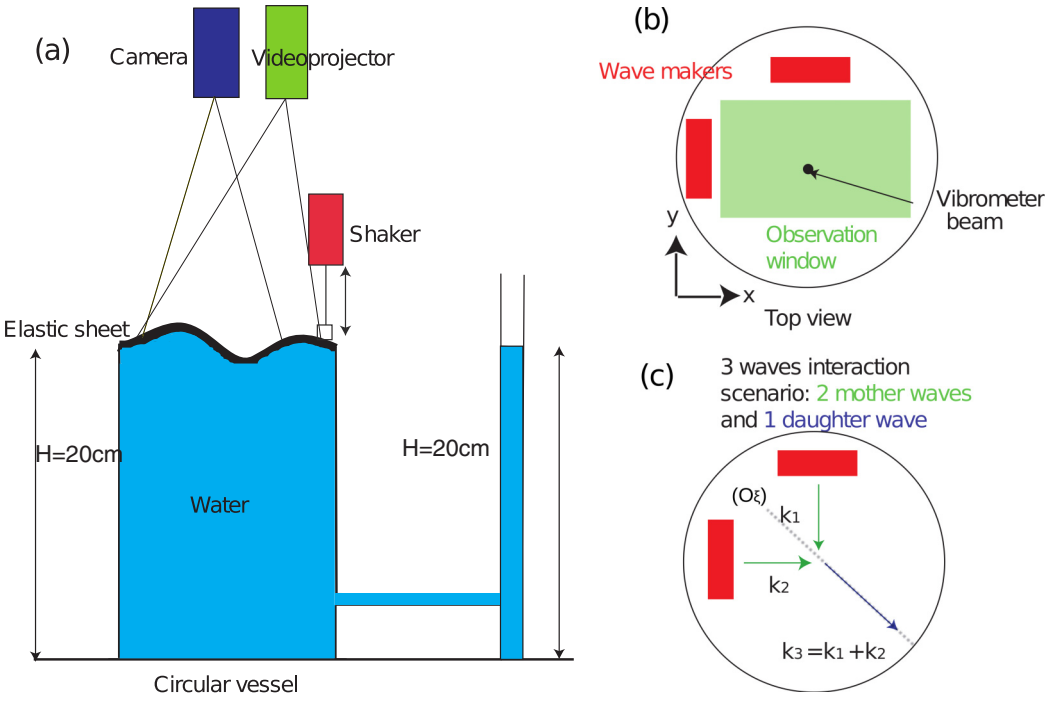

FIG. 1. Experimental setup: (a) side, (b) top view, and (c) wave interaction principle.

with $U_3 = \partial\omega_3/\partial k_3$ being the group velocity of the daughter wave. Noting that ϕ is independent of ξ for resonance conditions, an integration of Eq. (11) finally leads to

$$a_3^S(\xi) = a_1 a_2 \frac{\gamma_3 \sin\phi}{\delta_3} K(\xi), \tag{12}$$

where $K(\xi) = 1 - \exp[-\delta_3(\xi - \xi_0)/U_3]$ and ξ_0 is the coordinate defined by $a_3(\xi_0) = 0$. This factor $K(\xi)$ simply expresses the damping of the daughter-wave amplitude with distance ξ from its origin ξ_0. Note that this solution was first obtained in the context of three-wave interactions among capillary waves by Haudin *et al.* [20]. Equation (12) will be used afterwards to make a quantitative comparison with the experimental data of Sec. IV. This relation between wave amplitudes will be tested experimentally, as well as the occurrence of a phase locking (total phase ϕ independent of time).

III. EXPERIMENTAL SETUP

The experimental setup is similar to that described by Deike *et al.* [26] and is shown in Figs. 1(a) and 1(b). It consists of a cylindrical vessel of radius $R = 20$ cm filled with water up to a height $H = 20$ cm. An elastic latex sheet is stuck on the top circular side of the container. We carefully checked that no air bubbles were trapped between the sheet and the water. The measured physical properties of the latex sheet are thickness $h = 0.35$ mm, Young's modulus $E = 1.05\ 10^6$ N/m^2, and Poisson modulus $\nu \approx 0.5$ (industrial latex was provided by Eurocatsuits) and the bending modulus is $D = Eh^3/12(1-\nu^2)$. It was shown previously that the pressure only due to the weight of the elastic sheet with no water beneath yields to a static tension $T_s^0 = 5$ N/m of the elastic sheet due to its sticking on the vessel [26]. The transition between gravity and tensional waves is then $\lambda_{gT} \simeq 10$ cm, of the order of the vessel size and the observation window. Moreover, bending waves will occur for

wavelengths smaller than $\lambda_{TD} \simeq 1$ cm, leading to a transition $f_{TD} \approx 250$ Hz. Thus, only tension and bending waves are observed here.

Waves on the sheet are generated by the vertical motion of two rectangular wave makers (186×10 mm^2) driven by an electromagnetic shaker (LDS V201), as shown in Fig. 1(b). The two wave makers are making an angle of approximately 95°, as shown in Fig. 1(b), the angle being fixed by experimental constraints. Both wave makers are started at the same time $t = 0$ s by a sinusoidal forcing at a given frequency f_j. Thus the displacement of each wave maker is $a_j = a_j^0 \sin(\omega_j t)$, with $j = 1,2$. The wave maker acceleration is measured by an accelerometer (BK 4393) fixed on the wave maker. In all the experiments presented here, the amplitude of the two mother waves are chosen to be the same, equal to $a_{0,j} = a_0$, $j = 1,2$; therefore a_0 is the forcing amplitude. The forcing frequencies are chosen as $f_j = \omega_j/(2\pi) \in [35 : 100]$ Hz, with $\Delta f = |f_2 - f_1| \in [8 : 16]$ Hz.

We perform two types of wave field measurements. (i) The full three-dimensional (3D) spacetime-resolved wave field is measured by using a fast Fourier profilometry technique [40] recently used on hydroelastic waves [26], elastic waves on a metallic plate [41], or for gravity-capillary waves on a fluid surface [42]. Fringes with interfranges of 1 mm are projected on the sheet surface by a high-resolution video projector (Epson TW3000), and the spacetime evolution of the fringe deformations enable us to reconstruct the velocity normal to the free surface $v(x,y,t)$ with a fast camera (Phantom V9) recording at 1000 fps during $\mathcal{T} = 4$ s. The size of the recorded images, centered in the middle of the sheet, is 25×18 cm^2. From the movie of $v(x,y,t)$, one computes the power spectrum density of transverse velocity $S_v(k_x,k_y,f)$ from multidimensional Fourier transform. By integrating $S_v(\mathbf{k},f)$ over all directions of the wave vector $\mathbf{k}$, we also obtain $S_v(k = ||\mathbf{k}||, f)$, with $k \equiv (k_x^2 + k_y^2)^{1/2}$ the wave number. (ii) The temporal one-point measure of the normal velocity is achieved with a Doppler velocimeter (Polytech OPV 506), sampled at 10 kHz. The location of the spatial measurement window and the vibrometer location are indicated on Fig. 1 b. Both measurements are not performed simultaneously for technical reasons. The spatial measurement allows us to characterize the wave propagation geometry and lasts 4 s, while the one-point measurement is used to perform a time-frequency analysis and lasts 10 s. In both cases, the measure starts at $t = 0$ when the wave makers are turned on in order to capture the beginning of the forcing and the transient regimes. The stationary regime is reached in about 1s. The same experiment is repeated $N = 10$ times in the vibrometer case in order to realize ensemble average (denoted by $\langle\cdot\rangle$). This protocol increases the statistics, reduces the signal-to-noise ratio, and improves the time-frequency analysis.

Forcing amplitudes are between $a_0 \in [0.01,0.1]$ mm in order to observe weakly nonlinear effects. The very high sensibility of the laser vibrometer allows us to capture a daughter wave amplitude of the order of 0.1–1 μm. Extreme care is thus necessary when these experiments are performed. Note that we measure vertical velocities $v = \partial\eta/\partial t$. The theoretical results are given as function of the wave height η and the link for an angular frequency ω_i between $\hat{\eta}(\omega)$ and $\hat{v}(\omega)$ in Fourier space is $|\hat{v}(\omega_j)| = \omega_j|\hat{\eta}(\omega_j)|$.

IV. EXPERIMENTAL RESULTS

A. Spatial observations of three-wave resonant interactions

The analysis of the temporal $v(t)$ and spatial $v(x,y,t)$ wave-field data, as well as the spacetime spectrum $S_v(\mathbf{k},f)$ allows us to analyze the appearance of a daughter wave from a couple of mother waves, satisfying both resonant conditions of Eq. (5). We present these observations for a given couple of initial frequencies, $f_1 = 35$ Hz and $f_2 = 43$ Hz but the presented phenomenology is valid for all studied cases.

Figures 2(a) and 2(b) show observation of the wave field $v(x,y,t)$, at the beginning of the experiment, measured by the spatial method. Two wave trains are observed, coming from the two wave makers [Fig. 2(a)], close to a 95° angle, and with wave vectors $\mathbf{k}_1$ and $\mathbf{k}_2$, respectively. The two waves meet in the middle of the observation window [Fig. 2(b)]. When the two wave trains meet, they generate a modulated wave field, with crests and troughs in the surface-velocity distribution

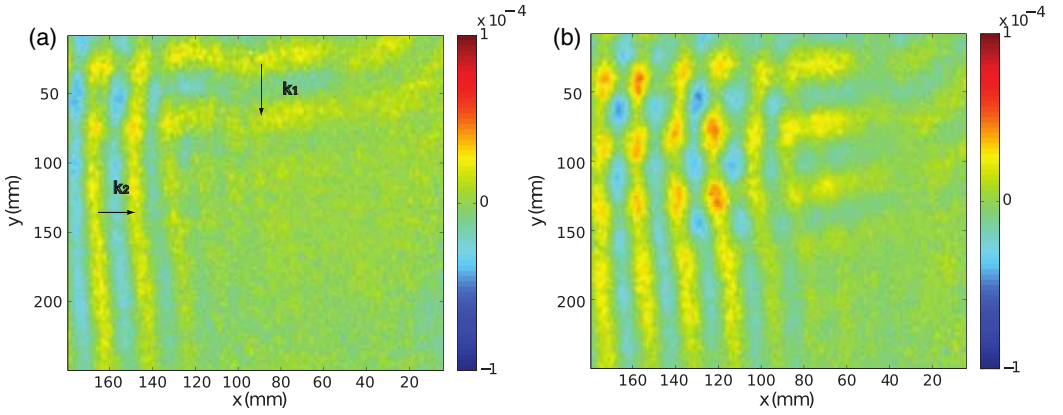

FIG. 2. (a), (b) Wave vertical velocity $v(x,y,t)$ (linear color scale is v in m/s) just after (a) the forcing is started and (b) later on. Two quasi plane waves (a) are first seen and (b) interact, leading to a more complex field. $f_1 = 35$ Hz and $f_2 = 43$ Hz.

corresponding mainly to wave superposition. An analysis in the Fourier space is necessary to properly identify wave interaction and detect the daughter wave at the resonant frequency.

Figure 3(a) shows the spacetime spectrum of the wave velocity $S_v(k,f)$ integrated over the angles and over the total time measurement. The two mother-wave frequencies f_1 and f_2 as well as the daughter-wave frequency f_3 are clearly visible and are indicated with dashed lines as well as the wave-numbers k_j. The first harmonics $2f_1$ and $2f_2$ are also clearly visible. These modes are all localized around the curve corresponding to the dispersion relation [Eq. (4)], with $T = T_s$ the static tension of the sheet, showing that hydroelastic waves propagates following the linear dispersion relation. Note that the spot visible around 60 Hz at low wave number is the blinking of the video projector. Note also that the harmonics of the forcing frequency are observed on the dispersion relation $[2\omega_i, k(2\omega_i)]$, and not as bound waves $[2\omega_i, 2k(\omega_i)]$ as for pure gravity waves [23,42,43]. The resonant interaction mechanism for gravity waves involve four-wave interaction and the bound waves appear as three-wave nonresonant interaction in this system [43]. In the case of capillary waves, or hydroelastic waves, the resonant mechanism involves three-wave interactions, and no bound waves are observed; see also Refs. [20,26,44]. It is possible that the occurrence of three-wave resonant interaction masks, or prevents, the development of bound waves.

To discuss the propagation directions, we compute the spatial spectrum at given frequencies f_j, $S_v(k_x,k_y,f_j)$, as shown on Figs. 3(b)–3(d), for (b), (c) the two mother waves and (d) the daughter wave. Figure 3(b) shows the spatial spectrum at the first mother wave frequency $S_v(k_x,k_y,f_1)$. The propagation direction clearly appears, the energy is mainly localized in the $y > 0$ direction, which is given by the forcing. The wave vector $\mathbf{k}_1$ is indicated in Fig. 3(b). Energy is also observed for other directions due to wave reflection and wave interactions (the spectrum being calculated over the total time of the experiment). Similar observations are made for the second mother wave, as shown in Fig. 3(c), with $S_v(k_x,k_y,f_2)$. Here, the main direction is $x < 0$ (as defined by the forcing direction in Fig. 2) and $\mathbf{k}_2$ is identified. Finally, the spatial spectrum at the daughter-wave frequency $S_v(k_x,k_y,f_3)$ and its wave vector $\mathbf{k}_3$ is identified in Fig. 3(d): energy is localized in the direction given by $\mathbf{k}_3 = \mathbf{k}_1 + \mathbf{k}_2$, within the measurement accuracy.

Note that a slight difference is observed in Fig. 3(d) between the experimental and theoretical values of the wave number $1/\lambda_3$, respectively, 51 m^{-1} (white arrow) and 56 m^{-1} (radius of the black circle). This difference of 5 m^{-1} is within the nonlinear broadening of the dispersion relation. Indeed, the typical width $[\delta(\lambda_3^{-1}), \delta f_3]$ of the dispersion relation [Fig. 3(a)] centered on the point (λ_3^{-1}, f_3) is roughly (14 m^{-1}, 4.5 Hz). This spectrum broadening is usually ascribed to the typical nonlinear scale of interacting waves [42]. However, one should be careful since this difference is

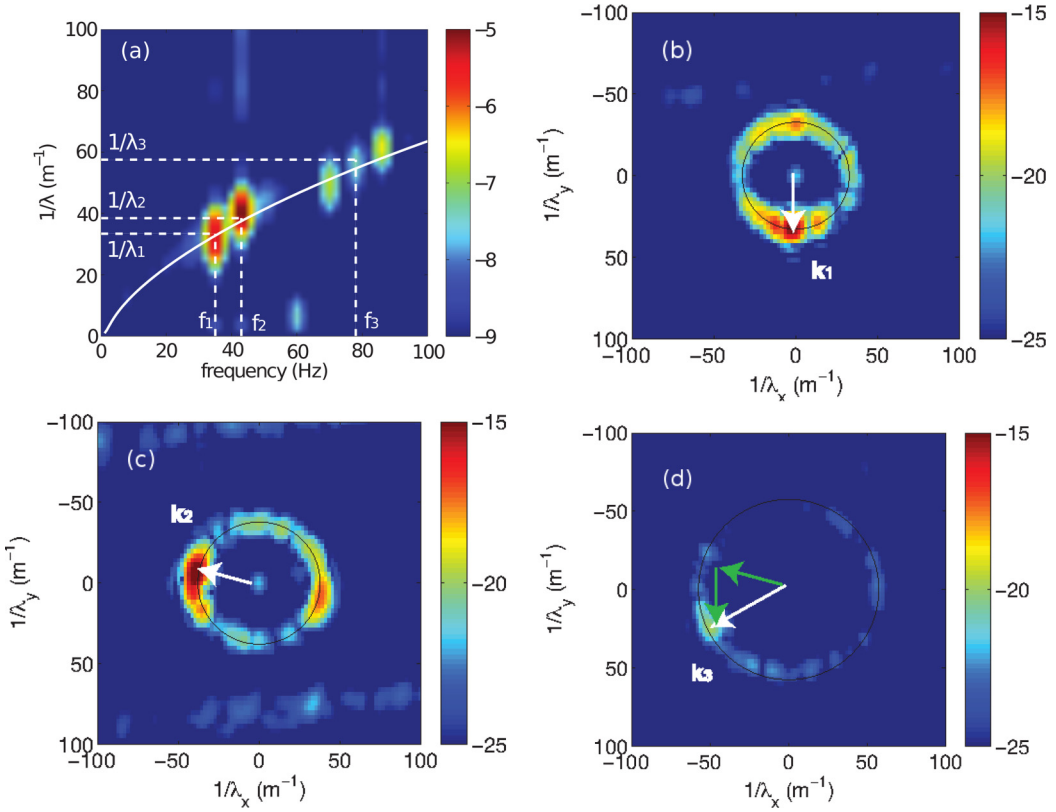

FIG. 3. (a): Angle-integrated spacetime vertical velocity spectrum $S_v(1/\lambda, f)$. White solid line is the linear dispersion relation (4), $\omega^2 = \frac{T}{\rho}k^3 + \frac{D}{\rho}k^5$, with $T = 5$ N/m. White dashed lines are the frequencies f_1, f_2, and f_3, respectively, and the corresponding wave numbers. (b) Spatial spectrum at frequency f_1: $S_v(k_x, k_y, f_1)$. (c) Spatial spectrum at frequency f_2: $S_v(k_x, k_y, f_2)$. (f) Spatial spectrum at frequency f_3: $S_v(k_x, k_y, f_3)$.In panel (d) the relation $\mathbf{k}_3 = \mathbf{k}_1 + \mathbf{k}_2$ is shown. In panels (b)–(d), the solid black circle has a radius $|\mathbf{k}_j|$ given by the linear dispersion relation $|\mathbf{k}_j|(\omega_j)$. The white arrow shows the wave vector $\mathbf{k}_j$. $f_1 = 35$ Hz and $f_2 = 43$ Hz. The color bar is the spectrum amplitude log scaled.

also close to our spatial spectral resolution [defined as $\Delta k/(2\pi) =$ the inverse of the image size; ~ 5 m^{-1}]. Finally, this slight difference may be also attributed to the near-resonance conditions of our experiments. Indeed, the crossing angle between the two mother waves is close to 95°, whereas the theoretical angle for exact resonance is close to 75° by using Eqs. (4) and (5).

Thus, the frequency and wave vector of the daughter wave are found to satisfy the resonance conditions within the spatial resolution, i.e., $\mathbf{k}_1 + \mathbf{k}_2 = \mathbf{k}_3 + \Delta\mathbf{k}$ with $\Delta k/k_3 < 0.1$, and $\omega_1 + \omega_2 = \omega_3$.

B. Time-frequency spectrum

We now compute the time-frequency spectrum $S_v(t, f)$ by using the one-point vibrometer data, which is possible thanks to the high-frequency sampling rate.

Figure 4 shows the time-frequency spectrum $\langle S_v(t, f)\rangle$, for one typical experiment, with the forcing frequencies f_1 and f_2 clearly visible and present from the beginning of the experiment ($t = 0$ when the wave makers are started). After a short transient regime, their amplitudes remain roughly constant. The resonant frequency created by three-wave interaction is also visible at $f_3 = f_1 + f_2$ as well as the forcing first harmonics at $2f_1$ and $2f_2$, appearing shortly after the forcing starts (≈0.1 s).

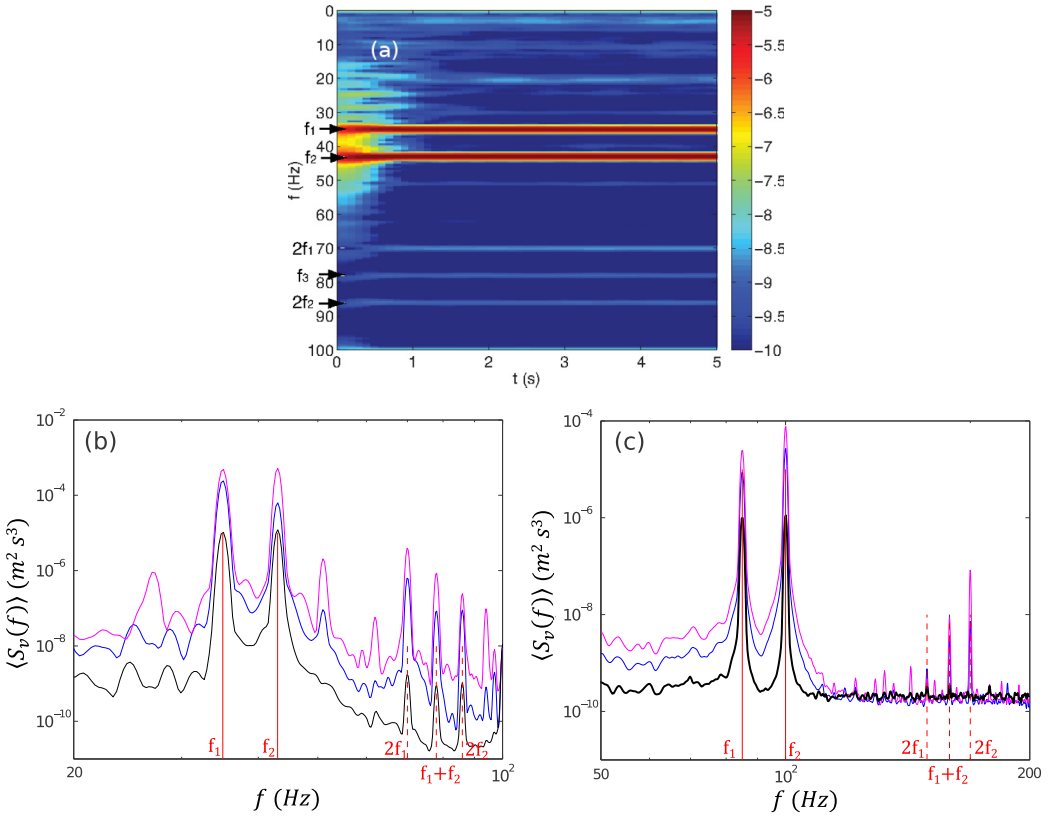

FIG. 4. Time-frequency spectrum $\langle S_v(t,f)\rangle$; color is log scaled. $f_1 = 35$ Hz and $f_2 = 43$ Hz are visible from $t = 0$ while a slight delay is observed before the appearance of the daughter wave at f_3. The amplitude at f_3 remains much smaller than that at f_1 and f_2. Energy at the harmonics of the forcing; $2f_1$ and $2f_2$ is also visible. (b), (c) Frequency spectrum $\langle S_v(f)\rangle$ for different mother-wave forcing amplitudes, and for two couples of mother-wave frequencies [left of panel (b)] $f_1 = 35$ Hz and $f_2 = 43$ Hz and [right of panel (c)] $f_1 = 85$ Hz, $f_2 = 100$ Hz. f_1 and f_2 are indicated by solid vertical lines. Dashed lines are $2f_1$, $f_3 = f_1 + f_2$, and $2f_2$ (from left to right).

Figures 4(b) and 4(c) show the frequency spectrum $\langle S_v(f)\rangle$, from the time integration of the time-frequency spectrum over the total experimental time (10 s), with increasing forcing amplitude of the mother waves, a_0, for two couples of frequencies. The mother-wave frequencies, as well as their harmonics, and the daughter-wave frequency are clearly identified. The two mother waves have comparable amplitudes $a_1 \approx a_2$, which are much larger than the daughter-wave amplitude, a_1,$a_2 \gg a_3$ or than the amplitude of the forcing harmonics. The daughter-wave amplitude is found to increase when the mother-wave amplitudes are increased. Note that harmonics of the forcing at $2f_1$ and $2f_2$ are nonlinearly generated by the wave makers forcing. A peak at $f_1 - f_2$ is also observed with a smaller amplitude (not shown). Although its generation is also related to a three-wave mechanism, the corresponding wavelength (around 9 cm for 8 Hz and 6 cm for 15 Hz) is close to the tank dimensions.

C. Evidence of phase locking

The mother- and daughter-wave phases $\phi_j(t) = \mathbf{k}_j \cdot \mathbf{x}_p - \omega_j t + \varphi_j$ are estimated by band passing the amplitude signal $\eta(t)$, recorded at the probe position $\mathbf{x}_p$, around the target frequency f_j (bandpass filter is ± 1 Hz), and by then performing an Hilbert transform. The Hilbert transform gives us an

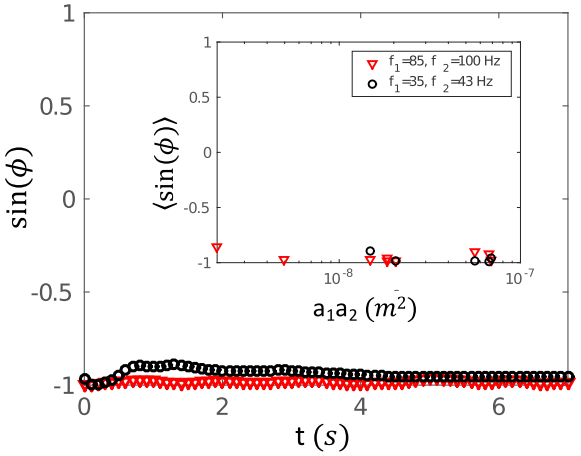

FIG. 5. Temporal evolution of the sine of the total phase $\phi(t) = \phi_1(t) + \phi_2(t) - \phi_3(t)$ for two couples of mother-wave frequencies. A phase locking is observed with $\phi \approx -\pi/2$, as predicted theoretically. Inset shows ensemble- and time-averaged value of the sine of the total phase, $\langle \sin\phi \rangle$, for different mother-wave amplitudes. Phase locking is observed in all experiments.

estimate of the wave amplitude a_j and the wave phase ϕ_j at frequency f_j. The phase of each wave $\phi_j(t)$ obviously changes with time. On the contrary, the signed sum of the phases defined by $\phi(t) = \phi_1(t) + \phi_2(t) - \phi_3(t)$ is found to be independent of time, as shown in Fig. 5 where the temporal evolution of $\sin\phi(t)$ is displayed for two couples of mother waves. After the wavefront has passed the probe, the total phase is found to be locked at $-\pi/2$ (i.e., $\sin\phi \approx -1$). The phase locking observed here is in very good agreement with the prediction in Sec. II C. The $-\pi/2$ value means that the energy transfer to the daughter wave is maximum [see Eq. (9)]. As shown in the inset of Fig. 5, a similar phase locking is observed regardless of the mother-wave amplitudes (provided that $a_3 \ll a_1, a_2$), and for the two tested couples of mother-wave frequencies. Note that, here, the time- and ensemble-averaged value of the phase is plotted. Phase locking is a second evidence of the generation of a daughter wave by resonant interactions.

D. Temporal evolution of daughter- and mother-wave amplitudes

The amplitude of the wave at frequency f_j can also be evaluated from the time-frequency spectrum of the velocity,

$$a_i(t) = v_i(\omega_i, t)/\omega_i, \tag{13}$$

$$v_i(\omega_i, t) = \sqrt{2 \int_{\omega_i - \kappa_\omega}^{\omega_i + \kappa_\omega} \langle S_v(u,t) \rangle du}, \tag{14}$$

and κ_ω is the width at half amplitude of the spectrum of the peak at frequency ω_j (typically $\kappa_\omega \approx 2\pi$ rad^{-1}). We have checked that evaluating the wave amplitude either by Hilbert transform or by the spectrum is equivalent. The time evolution of the mother-wave amplitudes $a_1(t)$ and $a_2(t)$, as well as the daughter-wave amplitude $a_3(t)$ are shown in Figs. 6(a) and 6(b) for a given initial mother-wave amplitude $a_0 \equiv a_1(t=0) = a_2(t=0)$. For all frequencies, a stationary value is reached after roughly one second. We observe that $a_1, a_2 \gg a_3$ is true for all times. However, the amplitudes of the mother waves are not constant with time during the growing of the daughter wave. Note that the growth of the forcing harmonics $2f_1$ and $2f_2$ is similar to that of the daughter wave

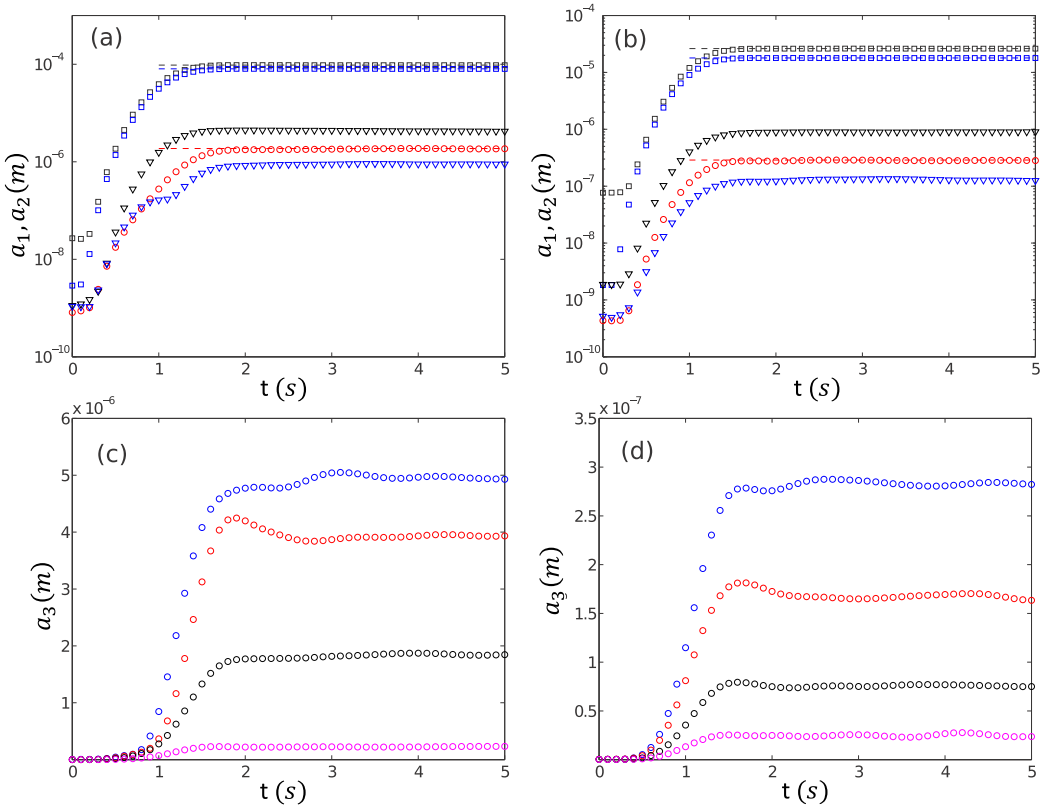

FIG. 6. (a), (b) Temporal evolution of the amplitudes of mother waves a_1 (□), a_2 (□), of daughter-wave a_3 (○), and of mother-wave harmonics at $2f_1$ (▽), $2f_2$ (▽) for fixed initial mother-wave amplitude $a_0 = a_1(t=0) = a_2(t=0)$, and for two couples of mother-wave frequencies (a) $f_1 = 35$ Hz, $f_2 = 43$ Hz and (b) $f_1 = 85$ Hz, $f_2 = 100$ Hz. (c), (d) Temporal evolution of the daughter-wave amplitude $a_3(t)$ for different initial amplitudes a_0 (from bottom to top). $f_1 = 35$ Hz and $f_2 = 43$ Hz (g); $f_1 = 85$ Hz and $f_2 = 100$ Hz (h). Dashed lines correspond to the stationary values a_3^S.

f_3. Finally, Figs. 6(c) and 6(d) show $a_3(t)$ for increasing mother-wave amplitudes a_0. For all values of a_0, a_3 first grows rapidly, and then reaches a stationary value a_3^S.

E. Scaling of daughter-wave amplitude

Previously, by using local and spatiotemporal measurements, we obtained evidence of the formation of a daughter wave due to the three-wave resonant interaction. Spatial observations reveal that the resonance conditions [Eq. (5)] are fulfilled within the measurement accuracy. After the early stage of the interaction where the mother and daughter wave grow rapidly, they reach a stationary value, while the total phase of the system experiences phase locking, as expected theoretically.

We now perform a quantitative comparison between the experimental data and the theoretical relation between stationary wave amplitudes [Eq. (12)]. To wit, we plot in Fig. 7 the experimental value of the rescaled daughter-wave amplitude $a_3^S \delta_3/[\gamma_3 \sin(\phi) K(\xi)]$ as a function of the forcing parameters, i.e., the product of the stationary mother-wave amplitudes $a_1 a_2$, for all experiments performed. This rescaling uses the measurements of a_3^S, of the total wave phase ϕ of the damping rate δ_3, the experimental estimation of the interaction coefficient γ_3 by using Eq. (7), and the spatial factor $K(\xi)$. $K(\xi) = 1 - \exp[-\delta_3(\xi - \xi_0)/U_3]$ is estimated by using the group velocity of the daughter wave, $U_3 = \partial\omega_3/\partial k_3$ computed from the linear dispersion of Eq. (4), and ξ inferred from

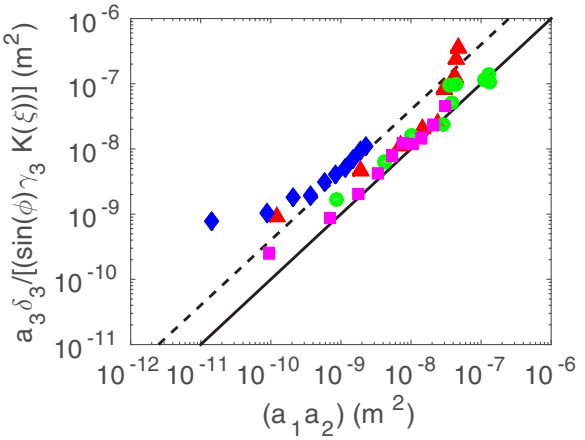

FIG. 7. Rescaled daughter-wave amplitude $a_3^S\delta_3/[\gamma_3 \sin(\phi)K(\xi)]$, as a function of a_1a_2. Experimentally, $\sin(\phi) = -1$, and $\delta(k_3)$, γ_3 and $K(\xi)$ are estimated as explained in the text. Various couples of mother-wave frequencies: ($\triangle$) $f_1 = 35$, $f_2 = 51$ Hz; ($\circ$) $f_1 = 35$, $f_2 = 43$ Hz; ($\square$) $f_1 = 55$, $f_2 = 63$ Hz; ($\diamond$) $f_1 = 85$, $f_2 = 100$ Hz. Solid line has a slope 1 and corresponds to the theoretical prediction of Eq. (12). Dashed line has a slope one with a prefactor of four. The full and open symbols are, respectively, for the theoretical (90°) and observed (75°) angle between the mother waves and cannot be distinguish on the figure.

the probe location from the origin ξ_0. The damping rate of hydroelastic waves had already been measured in a previous study [26] and is given by $\delta(k) = k/(4\pi C)$ with $C = 3.2$ s/m.

This dissipation rate was measured in Ref. [26] up to $1/\lambda \approx 80$ m^{-1}, corresponding to $f \approx 150$ Hz, while the highest tested daughter-wave frequency in the present experiment is $f = 185$ Hz. In a recent study, Ref. [45] measured the attenuation of flexural gravity waves by using a similar elastic sheet as the one considered here and reported decay rates compatible with the model from Ref. [46] for a surface boundary layer under an inelastic sheet. However, in Ref. [45], the sheet is free to move at the boundary while our sheet is clamped on the side of the tank. When we compare the measured decay rate extrapolated at higher frequencies with the decay rate in a surface boundary layer from Refs. [45–48], we observe that the surface boundary layer dissipation from Refs. [45–47] only becomes larger than our extrapolated dissipation for very high frequencies $1/\lambda > 200$ m^{-1} ($f > 800$ Hz), which are not reached in the present experiment. This means that other sources of dissipation are necessary to explain the observed dissipation, as already discussed in Ref. [26]: dissipation at the boundaries due to the clamping of the sheet (similar to the case of flexural waves on an elastic plate discussed by Refs. [49,50]), or viscoelastic dissipation.

According to the resonant wave interaction theory of Eq. (12), all data in Fig. 7 should collapse onto the straight line of slope one (solid line). Indeed, this prediction is in good agreement with the experimental data over more than one order of magnitude in a_1a_2 and with no fitting parameter. Note that a significant departure is observed for the highest tested frequency couple (offset of a factor of four shown by the dashed line), which could be attributed to an additional dissipation at high frequency. Moreover, for the extreme values of the forcing, some discrepancies are visible. For strong amplitude, this may be ascribed to the growth of other modes in the system (harmonics and other interactions) while, at low amplitude, there might not be enough energy to permit nonlinear exchanges between the modes. Finally, the interaction coefficient γ_3 has been estimated by using the values of the crossing angle between mother waves either experimental, 95° (open symbols in Fig. 7) or predicted theoretically to be at exact resonance, i.e., 75°, (solid symbols), with no visible difference in Fig. 7. The open and full symbols are also superposed on the figure. To sum up, the scaling of the daughter-wave amplitude with the mother-wave amplitudes is found to be in reasonable

agreement with the prediction of resonant wave interaction theory with no fitting parameter, while the geometry of the mother waves do not perfectly match the resonance conditions.

V. CONCLUSIONS

We have experimentally studied three-wave interactions in a system of hydroelastic waves propagating over a floating elastic sheet. We observe a daughter wave generated from the nonlinear interaction among two mother waves of almost perpendicular directions. The frequency and the wave vector of the daughter wave are found to satisfy the resonance conditions within the measurement accuracy. The daughter-wave amplitude is also found to be reasonably well described by the resonant wave interaction theory with no fitting parameter. This three-wave resonant interaction mechanism is observed in a range of scales where both tension and bending are necessary to described the wave dynamics. Further experimental works will be focused on changing the crossing angle between mother waves to describe wave interactions from in-resonance to off-resonance conditions.

This work also opens further research prospects. Experiments on the spatial growth of these hydroelastic waves would be of interest together with experiments to investigate wave interactions in the case of flexural-gravity wave and purely flexural waves. Both cases are indeed of importance for ocean applications when describing the dynamics of floating ice sheets. Finally, a major challenge is to experimentally study the development of resonant interactions, when the forcing amplitude is further increased, to observe the transition to a wave turbulence regime.

ACKNOWLEDGMENTS

This work was supported by ANR Turbulon Grant No. 12-BS04-0005. The authors thank J.-C. Bacri, B. Miquel, and F. Haudin for discussion, and A. Lantheaume for technical help. We thank the two anonymous referees for helpful comments.

[1] S. Nazarenko, *Wave Turbulence* (Springer-Verlag, Berlin, Heidelberg, 2011).
[2] A. C. Newell and B. Rumpf, Wave turbulence, Annu. Rev. Fluid Mech. **43**, 59 (2011).
[3] A. Bers, D. J. Kaup, and A. H. Reiman, Nonlinear Interactions of Three Wave Packets in a Homogeneous Medium, Phys. Rev. Lett. **37**, 182 (1976).
[4] D. J. Kaup, A. Reiman, and A. Bers, Space-time evolution of nonlinear three-wave interactions. I. Interaction in a homogeneous medium, Rev. Mod. Phys. **51**, 275 (1979).
[5] R. H. Enns and S. S. Rangnekar, The three-wave interaction in nonlinear optics, Phys. Status Solidi B **94**, 9 (1979).
[6] O. M. Phillips, On the dynamics of unsteady gravity waves of finite amplitude Part 1. The elementary interactions, J. Fluid Mech. **9**, 193 (1960).
[7] M. S. Longuet-Higgins, Resonant interactions between two trains of gravity waves, J. Fluid Mech. **12**, 321 (1962).
[8] A. D. D. Craik, Non-linear resonant instability in boundary layers, J. Fluid Mech. **50**, 393 (1971).
[9] M. D. Thomas and A. D. D. Craik, Three-wave resonance for free-surface flows over flexible boundaries, J. Fluids Struct. **2**, 323 (1988).
[10] B. S. Martin, W. Simmons, and C. Wunsch, The excitation of resonant triads by single internal waves, J. Fluid Mech. **53**, 17 (1972).
[11] A. D. McEwan, D. W. Mander, and R. K. Smith, Forced resonant second-order interaction between damped internal waves, J. Fluid Mech. **55**, 589 (1972).
[12] B. Bourget, T. Dauxois, S. Joubaud, and P. Odier, Experimental study of parametric subharmonic instability for internal plane waves, J. Fluid Mech. **723**, 1 (2013).

[13] G. Bordes, F. Moisy, T. Dauxois, and P. P. Cortet, Experimental evidence of a triadic resonance of plane inertial waves in a rotating fluid, Phys. Fluids **24**, 014105 (2012).
[14] L. F. McGoldrick, Resonant interactions among capillary-gravity waves, J. Fluid Mech. **21**, 305 (1965).
[15] L. F. McGoldrick, An experiment on second-order capillary gravity resonant wave interactions, J. Fluid Mech. **40**, 251 (1970).
[16] D. M. Henderson and J. L. Hammack, Experiments on ripple instabilities. Part 1. Resonant triads, J. Fluid Mech. **184**, 15 (1987).
[17] J. L. Hammack and D. M. Henderson, Resonant interactions among surface water waves, Annu. Rev. Fluid Mech. **25**, 55 (1993).
[18] L. F. McGoldrick, On Wilton's ripples: A special case of resonant interactions, J. Fluid Mech. **42**, 193 (1970).
[19] Q. Aubourg and N. Mordant, Nonlocal Resonances in Weak Turbulence of Gravity-Capillary Waves, Phys. Rev. Lett. **114**, 144501 (2015).
[20] F. Haudin, A. Cazaubiel, L. Deike, T. Jamin, E. Falcon, and M. Berhanu, Experimental study of three-wave interactions among capillary-gravity surface waves, Phys. Rev. E **93**, 043110 (2016).
[21] L. F. McGoldrick, O. M. Phillips, N. E. Huang, and T. H. Hodgson, Measurements of third-order resonant wave interactions, J. Fluid Mech. **25**, 437 (1966).
[22] M. S. Longuet-Higgins and N. D. Smith, An experiment on third-order resonant wave interactions, J. Fluid Mech. **25**, 417 (1966).
[23] F. Bonnefoy, F. Haudin, G. Michel, B. Semin, T. Humbert, S. Aumatre, M. Berhanu, and E. Falcon, Observation of resonant interactions among surface gravity waves, J. Fluid Mech. **805**, R3 (2016).
[24] G. During, C. Josserand, and S. Rica, Weak Turbulence for a Vibrating Plate: Can One Hear a Kolmogorov Spectrum? Phys. Rev. Lett. **97**, 025503 (2006).
[25] N. Mordant and B. Miquel, Observation of wave resonances: The thunder sheet reveals the core of weak turbulence (personal communication).
[26] L. Deike, J.-C. Bacri, and E. Falcon, Nonlinear waves on the surface of a fluid covered by an elastic sheet, J. Fluid Mech. **733**, 394 (2013).
[27] W. F. Simmons, A variational method for weak resonant wave interactions, Proc. R. Soc. London, Ser. A **309**, 551 (1969).
[28] J. B. Grotberg and O. E. Jensen, Biofluid mechanics in flexible tubes, Annu. Rev. Fluid Mech. **36**, 121 (2004).
[29] M. J. Shelley and J. Zhang, Flapping and bending bodies interacting with fluid flows, Annu. Rev. Fluid Mech. **43**, 449 (2011).
[30] E. Watanabe, T. Utsunomiya, and C. M. Wang, Hydroelastic analysis of pontoon-type VLFS: A literature survey, Eng. Struct. **26**, 245 (2004).
[31] V. A. Squire, J. P. Dugan, P. Wadhams, P. J. Rottier, and A. K. Liu, Of ocean waves and sea-ice, Annu. Rev. Fluid Mech. **27**, 115 (1995).
[32] V. A. Squire, Of ocean waves and sea-ice revisited, Cold Reg. Sci. Technol. **49**, 110 (2007).
[33] M. H. Meylan, L. G. Bennetts, C. Cavaliere, A. Alberello, and A. Toffoli, Experimental and theoretical models of wave-induced flexure of a sea ice floe, Phys. Fluids **27**, 041704 (2015).
[34] N. Peake and S. V. Sorokin, A nonlinear model of the dynamics of a large elastic plate with heavy fluid loading, Proc. R. Soc. London, Ser. A **462**, 2205 (2006).
[35] A. V. Marchenko and N. R. Sibgatullin, Evolution of wave packets in three-wave interaction in a heavy liquid under an ice covering, Fluid Dyn. **22**, 872 (1987).
[36] A. V. Marchenko and V. I. Shrira, Theory of two-dimensional nonlinear waves in liquid covered by ice, Fluid Dyn. **26**, 580 (1991).
[37] L. Landau and E. Lifshitz, *Theory of Elasticity* (Editions Mir, Moscow, 1951).
[38] J. W. Davys, R. J. Hosking, and A. D. Sneyd, Waves due to a steadily moving source on a floating ice plate, J. Fluid Mech. **158**, 269 (1985).
[39] R. M. S. M. Schulkes, R. J. Hosking, and A. D. Sneyd, Waves due to a steadily moving source on a floating ice plate. Part 2, J. Fluid Mech. **180**, 297 (1987).

[40] P. Cobelli, A. Maurel, V. Pagneux, and P. Petitjeans, Global measurement of water waves by Fourier transform profilometry, Exp. Fluids **46**, 1037 (2009).
[41] N. Mordant, Fourier analysis of wave turbulence in a thin elastic plate, Eur. Phys. J. B **76**, 537 (2010).
[42] E. Herbert, N. Mordant, and E. Falcon, Observation of the Nonlinear Dispersion Relation and Spatial Statistics of Wave Turbulence on the Surface of a Fluid, Phys. Rev. Lett. **105**, 144502 (2010).
[43] T. M. A. Taklo, K. Trulsen, O. Gramstad, H. E. Krogstad, and A. Jensen, Measurement of the dispersion relation for random surface gravity waves, J. Fluid Mech. **766**, 326 (2015).
[44] M. Berhanu and E. Falcon, Space-time-resolved capillary wave turbulence, Phys. Rev. E **87**, 033003 (2013).
[45] G. Sutherland, T. Halsne, J. Rabault, and A. Jensen, The attenuation of monochromatic surface waves due to the presence of an inextensible cover, Wave Motion **68**, 88 (2017).
[46] J. W. Miles, Surface-wave damping in closed basins, Proc. R. Soc. London, Ser. A **297**, 459 (1967).
[47] D. M. Henderson and J. W. Miles, Single-mode Faraday waves in small cylinders, J. Fluid Mech. **213**, 95 (1990).
[48] L. Deike, M. Berhanu, and E. Falcon, Decay of capillary wave turbulence, Phys. Rev. E **85**, 066311 (2012).
[49] B. Miquel, A. Alexakis, and N. Mordant, The role of dissipation in flexural wave turbulence: From experimental spectrum to Kolmogorov-Zakharov spectrum, Phys. Rev. E **89**, 062925 (2014).
[50] T. Humbert, O. Cadot, G. During, C. Josserand, S. Rica, and C. Touze, Wave turbulence in vibrating plates: The effect of damping, Europhys. Lett. **102**, 30002 (2013).